Investigating the dependence of mineral dust depolarization on complex refractive index and size with a laboratory polarimeter at 180.0° lidar backscattering angle

Alain Miffre[1], Danaël Cholleton[1], Clément Noël[1] and Patrick Rairoux[1]

[1]University of Lyon, Université Claude Bernard Lyon 1, CNRS, Institut Lumière Matière, F-69622, Villeurbanne, France

Correspondence to: Alain Miffre (alain.miffre@univ-lyon1.fr)

Abstract. In this paper, the dependence of the particles depolarization ratio (PDR) of mineral dust on the complex refractive index and size is for the first time investigated through a laboratory π-polarimeter operating at 180.0° backscattering angle and at (355, 532) nm wavelengths for lidar purposes. The dust PDR is indeed an important input parameter in polarization lidar experiments involving mineral dust. Our π-polarimeter provides sixteen accurate (< 1 %) values of the dust lidar PDR at 180.0° corresponding to four different complex refractive indices, studied at two size distributions (fine, coarse) ranging from 10 nm to more than 10 µm, and at (355, 532) nm wavelengths, while accounting for the highly irregular shape of mineral dust, which is difficult to model numerically. At 355 nm, the lidar PDR of coarser silica, the main oxide in mineral dust, is equal to (33 ± 1) % while that of coarser hematite, the main light absorbent in mineral dust, is (10 ± 1) %. This huge difference is here explained by accounting for the high imaginary part of the hematite complex refractive index. In turn, Arizona dust exhibits higher depolarization than Asian dust, due to the higher proportion in hematite in the latter. As a result, when the strong light absorbent hematite is involved, the dust lidar PDR primarily depends on the particles complex refractive index and its variations with size and shape are less pronounced. When hematite is less or not involved, the dust lidar PDR increases with increasing sizes, though the shape dependence may then also play a role. The (355, 532) nm wavelength dependence of the dust lidar PDR then allows discussing on the involved particle sizes, thus highlighting the importance of dual-wavelength (or more) polarization lidar instruments. We believe these laboratory findings will help improving our understanding of the challenging dependence of the dust lidar PDR with complex refractive index and size to help interpret the complexity and the wealth of polarization lidar signals.

1 Introduction

With worldwide annual emissions between 1000 to 3000 Tg (Monge et al., 2012), mineral dust is a highly important constituent of the atmosphere, which contributes to ice cloud formation by acting as a freezing nucleus and to the carbon cycle by fertilizing nutrient poor ecosystems such as the Amazon rainforest after long-range transport (Bristow et al., 2010). As underscored in the latest IPCC report (2021), mineral dust also contributes to the Earth's radiative budget through light scattering and

30 absorption, by reducing the amount of energy reaching the Earth's surface (Kosmopoulos et al., 2017). The radiative impact

31 associated with a Saharan dust storm has been recently quantified by Francis et al. (2022). This climatic impact is however

32 subject to large uncertainties, mainly due to the great complexity in size, shape and mineralogy of mineral dust. In the

33 atmosphere, the size distribution of mineral dust is mainly determined by the distance from the dust source region. Two freshly

34 uplifted dust aerosols may indeed exhibit different size distributions at far-range remote sites (Ryder et al., 2013), due to the

35 rapid removal of the largest particles by gravitational settling. Mineral dust particles also exhibit a high degree of complexity

36 in shape. Electron microscopic images (Kandler et al., 2011) indeed highlight the nonspherical and highly irregular shape of

37 mineral dust particles, with sharp edges, sometimes even surface roughness (Nousiainen, 2009). The mineral dust surface is

38 itself subject to photo-catalytic reactions leading even to new particle formation events (Dupart et al., 2012). The third degree

39 of complexity of mineral dust related to this study lies in its mineralogy. Mineral dust indeed consists in a heterogeneous

40 mixture of various chemical oxides among which the most predominant is silica oxide. Aluminum and iron oxides are also

41 present in proportions depending on the dust source region. As an example, the desert in Central Australia is iron oxides rich

42 (Bullard and White, 2002). This diverse mineralogy results in a diversity of complex refractive indices for mineral dust.

43

44 In the atmosphere, mineral dust is additionally often mixed with other aerosols. To face such a complexity, ground and satellite-

45 based polarization lidar instruments, based on light backscattering by nonspherical particles, have been developed

46 (Freudenthaler et al., 2009; Tesche et al., 2009; Sugimoto and Lee, 2006; Winker et al., 2009; Miffre et al., 2019; Hofer et al.,

47 2020; Hu et al., 2020) to discern the mineral dust contribution to two-component particles external mixtures, by applying lidar

48 partitioning algorithms such as the $1\beta + 1\delta$ algorithm (Tesche et al., 2009; Mehri et al., 2018). Such lidar-based retrievals are

49 however under-constrained and depend on prior knowledge regarding input parameters such as the lidar particles'

50 depolarization ratio (PDR). The lidar PDR quantifies the mineral dust particles deviation from isotropy and is key for aerosol

51 typing (Hofer et al., 2020; Burton et al., 2012). As explained in light scattering textbooks (Bohren and Huffman, 1983;

52 Mishchenko et al., 2002), it depends on the particles size, shape and complex refractive index. The size dependence of the

53 lidar PDR was studied in field by Hofer et al. (2020). The downside of such field measurements is that the observed aerosol is

54 nevertheless that of a particles mixture, which may induce some discrepancies in the retrieved dust lidar PDR (Miffre et al.,

55 2011). As an alternate, for accurate retrievals of the mineral dust lidar PDR, light backscattering numerical simulations have

56 been developed, by assuming a particles shape model such as the spheroidal shape model, computed with the T-matrix

57 numerical code (Mishchenko and Travis, 1998), as successfully applied for mineral dust during the SAMUM field campaign

58 (Müller et al., 2013) or, by considering more realistic shapes, based on stereograms, computed with the discrete-dipole-

59 approximation (Lindqvist et al., 2014; Gasteiger et al., 2011). Depending on the assumed shape model, the lidar PDR can be

60 very different with induced variations in the lidar-retrieved dust mass concentrations (Mehri et al., 2018). Recently, Luo et al.

61 (2022) and Huang et al. (2022) discussed on the ability of the spheroidal model to mimic the complex shape of mineral dust.

62 Likewise, Zubko et al. (2013) found spheroids inadequate for describing the dust particles' spectral dependence of the lidar

63 PDR. Such light scattering numerical simulations nonetheless rely on simplifying assumptions that should be carefully

64 checked. Laboratory experiments on natural dust samples at 180.0° lidar exact backscattering angle are then looked-for as they

65 provide quantitative evaluations of the mineral dust lidar *PDR* within experimental error bars. Indeed, in laboratory, the

66 retrieved lidar *PDR* is, by construction, that of pure mineral dust and the dependence of the dust lidar *PDR* with size and

67 mineralogy can be evaluated. Moreover, the complex shape of mineral dust is then accounted for. However, existing laboratory

68 light scattering experimental set-ups (Glen and Brooks, 2013; Järvinen et al., 2016; Gautam et al., 2020; Liu et al., 2020;

69 Kahnert et al., 2020; Gómez Martín et al., 2021) can only provide approximate values of the dust lidar *PDR* for the following

70 reasons:

71

72 – Such apparatuses operate at near backscattering angles only (< 180.0°), without covering the exact lidar

73   backscattering angle of 180.0°. The retrieved lidar *PDR* is then extrapolated to 180.0° following simplifying

74   numerical assumptions, ignoring the complexity in shape of mineral dust (Liu et al., 2020; Gómez Martín et al., 2021).

75   To provide accurate values of the dust lidar *PDR*, such assumptions must be carefully discussed as the lidar *PDR*

76   actually depends on the scattering angle in an unpredictable way, as underscored in light scattering textbooks (Bohren

77   and Huffman, 1983; Mishchenko et al., 2002), due to the complex shape of mineral dust. For that, a laboratory

78   measurement of the dust lidar *PDR* at 180.0° is mandatory.

79 – Also, most of the above apparatuses operate at a single wavelength, either 442, 488, 552, 632, 647 or 680 nm, which

80   differs from the (355, 532, 1064 nm) wavelengths which are applied in polarization lidar field experiments. As for

81   Raman lidars, such wavelength extrapolations up to the (355, 532, 1064 nm) lidar wavelengths are a source of

82   discrepancy as the dust lidar *PDR* actually depends on the complex refractive index, which is wavelength dependent

83   (Bohren and Huffman, 1983; Mishchenko et al., 2002). For that, a laboratory measurement at the lidar wavelengths

84   is mandatory.

85

86 In this paper, accurate values (< 1%) of the dust lidar *PDR* are provided from a laboratory π-polarimeter operating at 180.0°

87 lidar exact backscattering angle and at 355, 532 nm wavelength, to account for the importance of the spectral dependence of

88 the lidar *PDR* to better constrain lidar inversions and aerosol typing (Burton et al., 2016; Haarig et al., 2022). Since the

89 scattering angle and the wavelengths are determined for lidar purposes, we here investigate the dependence of the mineral dust

90 lidar *PDR* on the dust particles size and complex refractive index (*CRI*), the latter being particularly important as related to

91 light absorption. Light absorption by mineral dust preferentially occurs in the UV and VIS spectral domains, being nearly null

92 in the near-infrared spectral range (Di Biagio et al., 2019), noticeably in the presence of iron oxides (Formenti et al., 2014;

93 Caponi et al., 2017). By absorbing short-wave radiations, such oxides hence play a critical role in determining the overall

94 impact of dust aerosol on climate forcing (Go et al., 2022). We hence focused on 355 and 532 nm lidar wavelengths and

95 considered four dust samples differing in their *CRI*, thus in mineralogy: i) silica oxide (SiO_2), as the most abundant mineral

96 oxide present in mineral dust, ii) iron oxide (hematite, Fe_2O_3), as the main light absorbent present in mineral dust (Gautam et

97   al., 2020; Zong et al., 2021; Go et al., 2022), iii) and iv) two heterogeneous mixtures of the above two oxides in various

98   proportions, as detailed in Section 2. The dependence of the lidar PDR with size is then likewise investigating by accounting

99   for the fine and coarse modes of the particles size distribution (SD), to which lidar instruments are sensitive (Mamouri and

100   Ansmann, 2017), thus extending the size range of our previous laboratory findings (Miffre et al., 2016) to particles sizes larger

101   than 800 nm and to other mineralogy, as asked for in Tesche et al. (2019). According to the manufacturer, the size distribution

102   of our dust samples ranged from 10 nm to more than 10 µm in diameter. Our work provides sixteen laboratory-derived accurate

103   dust lidar PDR values, corresponding to four mineral dust samples differing in mineralogy, given at two SD (fine, coarse) and

104   at two wavelengths (355, 532 nm). Moreover, the role of the imaginary part of the hematite CRI, which may lead to

105   modifications in the lidar PDR, is here for the first time quantified and discussed.

106

107   The paper is structured as follows. In Section 2, the complex refractive indices and size distributions of our four dust samples

108   are presented. The laboratory π-polarimeter at 180.0° lidar backscattering angle is then presented in Section 3, together with

109   the dust lidar PDR retrieval methodology, derived from the scattering matrix formalism (Mishchenko et al., 2002). The main

110   findings are outlined in Section 4 where the sixteen values of dust lidar PDR are given and a discussion is proposed to

111   investigate the dependence of the dust lidar PDR on the imaginary part of the dust CRI. As in elastic lidar applications, we

112   here consider the elastic backscattering of electromagnetic radiation of wavelength λ by an ensemble of mineral dust particles

113   of complex refractive index $m = n + i\kappa$ embedded in ambient air.

114   **2. Mineral dust samples**

115   **2.1 Refractive indices**

116   Mineral dust is a complex mixture of several chemical oxides presenting various complex refractive indices. To investigate

117   the dependence of the dust lidar PDR on the complex refractive index (CRI), we consider the four following case studies :

118

119   –   Silica, or silicon oxide (SiO_2) is here considered as being the main pure chemical component present in mineral dust.

120   The silica CRI as given by Longtin et al. (1988) is equal to 1.546, hence exhibiting no absorptive component.

121   –   Iron oxide, or hematite (Fe_2O_3), is in contrast here selected as being a climatically significant light absorbent in the

122   shortwave spectral region, that can be transported far from source regions with similar efficiency as black carbon

123   particles (Lamb et al., 2021). It recently regained in interest with papers specifically dedicated to this constituent

124   (Gautam et al., 2020; Zong et al., 2021). Hematite is unique among all chemical oxides present in mineral dust due

125   its strong CRI. Both n and κ are large for hematite, with κ-values more than 100 times those of other soil mineral

126   components at lidar wavelengths. Hence, hematite dominates absorption while other minerals can be considered as

127   non-absorbing (Go et al., 2022). The real and imaginary part of the hematite CRI is provided by Scanza et al. (2015):

128   m = 2.13 + 0.94i at 355 nm wavelength (3.07 + 0.55i at 532 nm wavelength)..

129   –   Arizona Test Dust (hereafter called Arizona dust) is likewise considered as an example of natural mineral dust sample

130   that is a mixture of the above two oxides. According to the manufacturer (Power Technology Inc.), Arizona Test Dust

131   is composed of silica (68-76 %), while hematite is only weakly present in Arizona dust (2-5 %). In short, Arizona

132   dust is hence rather silica-rich. As given by the manufacturer, the Arizona dust CRI is $m = 1.51 + 10^{-3}i$, without

133   however any given on its spectral dependency. Effective medium theories can alternately be applied to account for

134   the sample inhomogeneity as calculated in Miffre et al. (2016), who arrived to $m = 1.57 + 10^{-2}i$ at 355 nm

135   wavelength and $1.55 + 5.10^{-3}i$ at 532 nm wavelength. As a result, the Arizona dust sample CRI is characterized by

136        $n \sim 1.5$ and a low absorbing component $\kappa \sim 5.10^{-3}$.

137   –   Asian dust is finally also considered as an important case study of natural mineral dust sample, presenting however a

138   lower proportion of silica (34-40 %) and a higher proportion in hematite (17-23 %). For Asian dust, we use a

139   commercial sample provided by Powder Technology (commercial name: Kanto Loam), commonly used as a dust

140   interferon in pollen light scattering measurements in Japan (Iwai, 2013), hence representative of observed atmospheric

141   Asian dust. In this way, we symmetrized our approach by dealing with both Arizona Test Dust and Asian Test Dust.

142   The CRI of Asian dust, evaluated from effective medium approximation, is m = 1.70 + 0.09i at 355 nm wavelength

143   and 1.72 + 0.03i at 532 nm wavelength. Hence, compared with Arizona dust, Asian dust is more hematite-rich and

144   hence exhibits a larger imaginary part for its CRI.

145

146 Other chemical oxides are also present in our dust samples in various percentages, but with negligible imaginary parts of CRI

147 compared with that of hematite. Investigating the PDR of these oxides is then beyond the scope of this paper. Their percentage

148 in (Arizona Test Dust, Asian Dust) is given for clarity: Al_2O_3 (11 %, 29 %), CaO (4 %, 1.5 %), K_2O (3.5 %, 0 %), Na_2O (2 %,

149 0 %), MgO (1.5 %, 5 %), TiO_2 (0.5 %, 2 %). The solid dust samples, provided by Sigma Aldrich and Powder Technology

150 manufacturers, were embedded in laboratory ambient air by using a solid dust generator supplied with dried compressed air

151 ($RH < 10$ %) to get dry solid dust particles embedded in laboratory ambient air at a constant number concentration, before

152 injecting the dust samples into the light scattering volume, as presented in Section 3.

153 **2.2 Size distribution (SD)**

154 For each above dust sample, we consider two size distributions (SD) to likewise investigate the dependence of the dust lidar

155 PDR on the particles size:

156   –   The coarser SD, represented in grey in Fig. 1. This SD is more representative of mineral dust particles close to dust

157   regions, although it does not cover the full range of large dust particles measured close to dust sources, showing

158   particles with diameters > 50 µm (Ryder et al., 2019),

159   –   A finer *SD*, plotted with a black line in Fig. 1, aimed at being more representative of mineral dust particles after long-
160   range transport, i.e. farther from the dust source regions.

161 The *SD* were obtained by adding / removing a cyclone to our experimental set-up allowing to add / remove particles with

162 diameter above 800 nm, thus exploring particles size ranges below and above 800 nm, as asked for in Tesche et al. (2019).

163 More precisely, the two considered SD correspond to a size distribution with and without coarse mode. The *SD* were measured

164 with an optical particles sizer (OPS 3330) coupled with a scanning mobility particles sizer (SMPS 3081), which selects the

165 dust particles as a function of their electric mobility, this latter quantity being diameter-dependent. As in Järvinen et al. (2016),

166 our size instruments could not measure dust particles with diameter above 10 μm. According to the manufacturer, such giant

167 particles (Ryder et al., 2019) are however present in our dust samples, at a low number concentration. The measured SD are

168 representative of what is observed in atmosphere, with a low number concentration of more than 10 μm particles, as observed

169 by Weinzierl et al. (2017). The particles *SD* displayed in Fig. 1 are in agreement with the specifications provided by the

170 manufacturers.
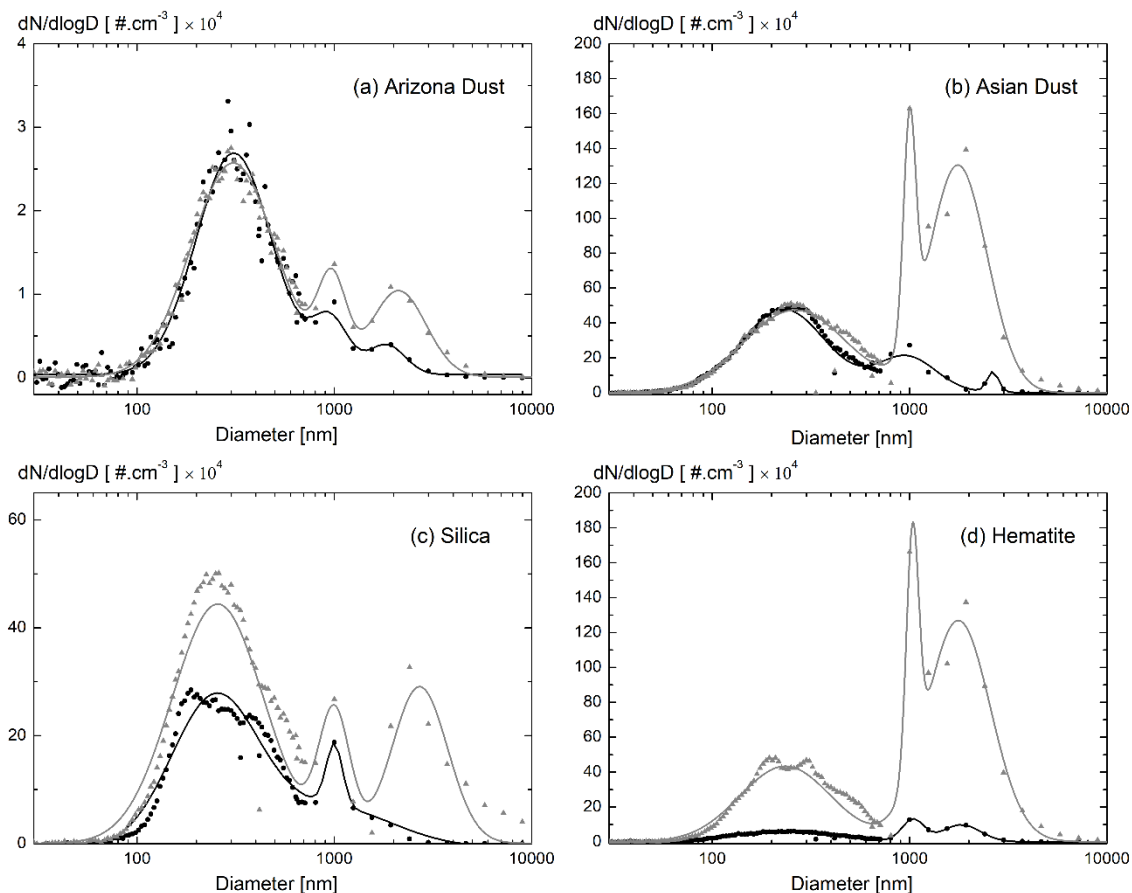
171

172 Figure 1: Dust particles size distributions (*SD*) for: (a) Arizona dust, (b) Asian dust, (c) Silica (SiO_2), (d) Hematite (Fe_2O_3) in
173 the presence / absence of the added cyclone (finer *SD*, in solid black) / (coarser *SD*, in dotted grey). The retrieved *SD*, obtained
174 by log-normal adjustments, agree with the specifications provided by the manufacturers.

3 Methodology

In this section, we detail our methodology for accurate laboratory evaluations of the dust lidar PDR at lidar exact backscattering angle of 180.0° for accurate lidar PDR-retrievals.

3.1 Scattering matrix formalism

The dust lidar PDR can be evaluated in the framework of the scattering matrix formalism (Mishchenko et al., 2002; Bohren and Huffman, 1983). In this formalism, the polarization state of the incident and scattered radiations are described by their respective Stokes vectors $\boldsymbol{St_i} = [I_i, Q_i, U_i, V_i]^\mathrm{T}$ and $\boldsymbol{St} = [I, Q, U, V]^\mathrm{T}$, defined with respect to the scattering plane, used as a reference plane (Mishchenko et al., 2002). The first Stokes component I corresponds to the light intensity, Q and U describe linear polarization, while V accounts for circular polarization. At a distance d from the mineral dust samples, if single-scattering and particles random orientation are assumed, for macroscopically isotropic and mirror-symmetric mediums, the incident and scattered Stokes vectors relate with a bloc-diagonal scattering matrix (Mishchenko et al., 2002; Bohren and Huffman, 1983):

$$\begin{pmatrix} I \\ Q \\ U \\ V \end{pmatrix} = \frac{1}{k^2 d^2} \begin{bmatrix} F_{11,\lambda}(\theta) & F_{12,\lambda}(\theta) & 0 & 0 \\ F_{12,\lambda}(\theta) & F_{22,\lambda}(\theta) & 0 & 0 \\ 0 & 0 & F_{33,\lambda}(\theta) & F_{34,\lambda}(\theta) \\ 0 & 0 & -F_{34,\lambda}(\theta) & F_{44,\lambda}(\theta) \end{bmatrix} \begin{pmatrix} I_i \\ Q_i \\ U_i \\ V_i \end{pmatrix} \tag{1}$$

Where the matrix elements $F_{ij,\lambda}(\theta)$ ($i, j = 1-4$) depend on the wavelength λ of the radiation (hereafter noted as a subscript) and carry information on the mineral dust particles size, shape and CRI. The scattering angle is $\theta = (\boldsymbol{k_i}, \boldsymbol{k})$, where $k = k_i = 2\pi/\lambda$ is the wave vector of the electromagnetic wave. In lidar applications, the scattering angle is equal to π (i.e. exact backscattering angle). To highlight the need for laboratory measurements at the specific 180.0° lidar backscattering angle, near backscattering angles (i.e. $\theta < \pi$) are also considered in this section. Indeed, at $\theta = \pi$, $F_{33,\lambda} = -F_{22,\lambda}$ and $F_{12,\lambda} = F_{34,\lambda} = 0$ (Zubko et al., 2013; David et al., 2013) while $F_{44,\lambda} = F_{11,\lambda} - 2F_{22,\lambda}$ due to the backscattering theorem (van de Hulst, 1957), so that Eq. (1) simplifies as follows for lidar applications:

$$\begin{pmatrix} I \\ Q \\ U \\ V \end{pmatrix} = \frac{1}{k^2 d^2} \begin{bmatrix} F_{11,\lambda}(\pi) & 0 & 0 & 0 \\ 0 & F_{22,\lambda}(\pi) & 0 & 0 \\ 0 & 0 & -F_{22,\lambda}(\pi) & 0 \\ 0 & 0 & 0 & F_{11,\lambda}(\pi) - 2F_{22,\lambda}(\pi) \end{bmatrix} \begin{pmatrix} I_i \\ Q_i \\ U_i \\ V_i \end{pmatrix} \tag{2}$$

As a result, it is only at elastic lidar exact backscattering angle ($\theta = \pi$) that $F_{12,\lambda} = 0$ so that the scattering matrix reduces to only two non-vanishing elements $F_{11,\lambda}(\pi)$ and $F_{22,\lambda}(\pi)$.

3.2 Lidar particles depolarization ratio *PDR*

The expression of the so-called particles linear depolarization ratio (*PDR*) at wavelength λ and scattering angle θ can be found in light scattering textbooks (Mishchenko et al., 2002; Schnaiter et al., 2012):

$$PDR_\lambda(\theta) = \frac{1 - F_{22,\lambda}(\theta)/F_{11,\lambda}(\theta)}{1 \pm 2F_{12,\lambda}(\theta)/F_{11,\lambda}(\theta) + F_{22,\lambda}(\theta)/F_{11,\lambda}(\theta)} \qquad (3)$$

where the positive (resp. negative) sign corresponds to *p*-polarized (resp. *s*-polarized) incident electromagnetic radiation. The PDR stated in Eq. (3) is the linear PDR, which can be related to the circular PDR if need be (Mishchenko et al., 2002). Since $F_{11,\lambda}$, $F_{12,\lambda}$ and $F_{22,\lambda}$ may vary with the scattering angle, depending on the dust sample, the dust *PDR* at near backscattering angles ($\theta < \pi$) differs from that obtained at specific lidar backscattering angle ($\theta = \pi$). The deviation of $F_{11,\lambda}$, $F_{12,\lambda}$ and $F_{22,\lambda}$ from their value at exact backscattering angle cannot be quantified since no analytical light scattering theory exists for such complex-shaped particles as mineral dust. Therefore, a laboratory experiment at specific lidar exact backscattering angle ($\theta = \pi$) is required for precise evaluations of the dust lidar *PDR*. At specific lidar backscattering angle of π, Eq. (3) becomes:

$$PDR_\lambda(\pi) = \frac{1 - F_{22,\lambda}(\pi)/F_{11,\lambda}(\pi)}{1 + F_{22,\lambda}(\pi)/F_{11,\lambda}(\pi)} \qquad (4)$$

Hence, accurate evaluations of the dust lidar *PDR* rely on accurate determinations of the ratio $F_{22,\lambda}/F_{11,\lambda}$ at specific lidar $\pi -$ angle. As for the ratio $F_{22,\lambda}/F_{11,\lambda}$, the dust lidar *PDR* is size, shape and refractive index dependent and this dependency is discussed in Section 4. Spherical particles, for which $F_{22,\lambda}/F_{11,\lambda} = 1$, lead to $PDR_\lambda(\pi) = 0$. In what follows, to ease the reading, the dust lidar *PDR* will be noted PDR_λ without reference to scattering angle ($\theta = \pi$).

3.3 Laboratory π-polarimeter for retrieving the lidar *PDR* of mineral dust

In (Miffre et al., 2016), for the first time to our knowledge, a laboratory π-polarimeter was built to address light backscattering by aerosol particles. We here recall its main characteristics for clarity. The aerosols π-polarimeter is schemed in Fig. 2. As in lidar applications, pulsed laser light is used to measure the time-of-flight taken by a laser pulse to reach the dust sample and be detected after light backscattering. The backscattering geometry is set by inserting a well-characterized polarizing beam splitter cube (*PBC*) between the emission and the dust samples, with a precision of 1 mm out of 10 meters to ensure the π-polarimeter covers the lidar exact backscattering direction with accuracy: $\theta = (180.0 \pm 0.2)°$. The laboratory aerosol π-polarimeter is actually composed of two identical polarimeters, one per wavelength, to evaluate the lidar PDR of a given dust sample at 355 and 532 nm wavelength simultaneously. Moreover, to decrease the retrieval uncertainty on the dust PDR, the polarization state of the backscattered radiation is analysed for a set of incident polarization states of the incident

232 light using a quarter-wave plate (QWP). To validate the laboratory π-polarimeter, we carefully checked that homogeneous

233 spherical particles, such as ammonium sulfate particles, which scatter light as described by the Mie theory (Bohren and

234 Huffmann, 1983), were indeed providing zero lidar PDR when following the methodology described in the below section.

235

236
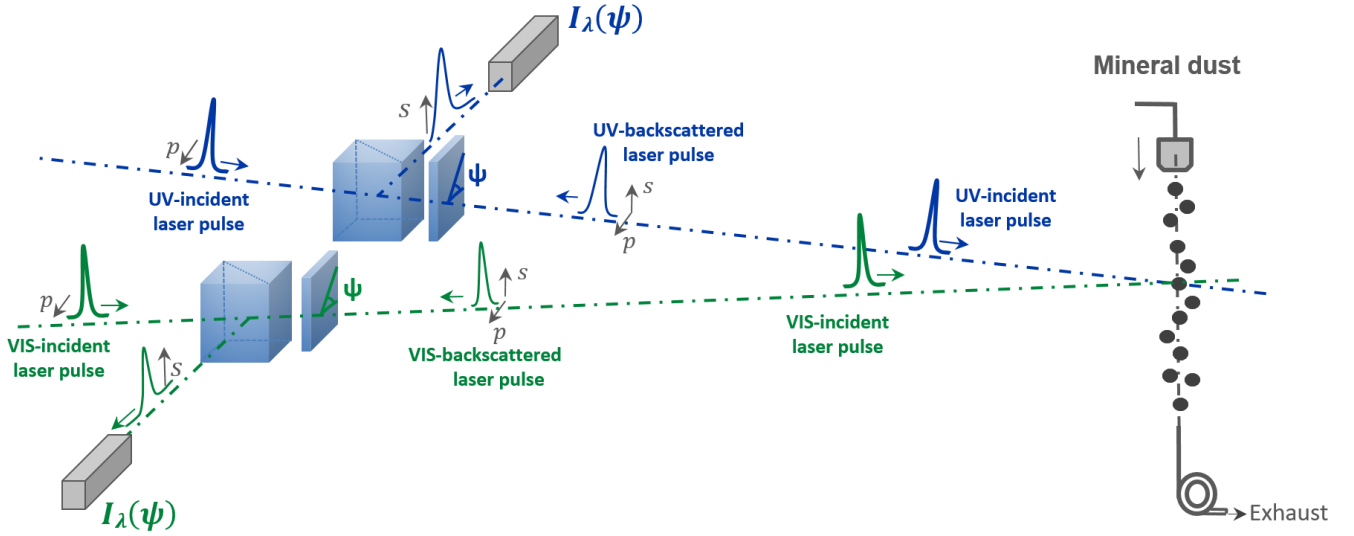
Figure 2: Scheme of the laboratory π-polarimeter operating at lidar exact backscattering angle of $(180.0 \pm 0.2)°$ allowing accurate retrievals of the lidar PDR at 355 and 532 nm wavelength simultaneously for an aerosol sample (Miffre et al., 2016). The (p, s) polarization components are defined with respect to the laser scattering plane and ψ is the angle between the fast axis of the QWP and the laser scattering plane, counted counter-clockwise for an observer looking from the PBC to the particles. The dust lidar PDR is then evaluated from the ratio $F_{22,\lambda}/F_{11,\lambda}$ at specific π-angle, following the methodology described in Section 3.4.

242 **3.4 Laboratory retrievals of mineral dust lidar PDR**

243   We can formulate the PDR measurements of dust particles, using successive Mueller matrices denoting to the optical

244 elements of the π-polarimeter and the scattering medium, encountered by the laser pulse from the laser source to the dust

245 particles sample then back to the light detector. The measured backscattered intensity is :

246

247 $$I_\lambda(\psi) = \frac{\eta_\lambda P_\lambda}{d^2} [1, 0, 0, 0]^T [\boldsymbol{PBC}][\boldsymbol{QWP}(-\psi)][\boldsymbol{F_\lambda}][\boldsymbol{QWP}(\psi)][\boldsymbol{PBC}](St_i) \qquad (5)$$

248

249 Where η_λ is the optoelectronics efficiency of the light detector and P_λ is the laser power density, while $(St_i) = [1, 1, 0, 0]^T$ is

250 the Stokes vector of the incident laser light. The expression of the dust backscattering matrix $[\boldsymbol{F_\lambda}]$ at wavelength λ is is given

251 in Eq. (2), while $[\boldsymbol{PBC}]$ and $[\boldsymbol{QWP}(\pm\psi)]$ are the Mueller matrices of the PBC and the QWP respectively (Shurcliff, 1962).

252 To develop Eq. (5), it is then advised to first calculate the raw vector $[1, 0, 0, 0]^T [\boldsymbol{PBC}][\boldsymbol{QWP}(-\psi)][\boldsymbol{F_\lambda}]$ then multiply it with

253 the Stokes vector of the incident laser light $[\boldsymbol{QWP}(\psi)][\boldsymbol{PBC}](St_i)$ equal to $[1, \cos^2(2\psi), -\sin(4\psi)/2, -\sin(2\psi)]^T$, with ψ

254 the modulation angle of the QWP. After a few calculations, the dust backscattered light intensity I_λ at wavelength λ is

255 calculated as shown in Eq. 6:

$$I_\lambda(\psi) = I_{\lambda,0} \times [a_\lambda - b_\lambda \cos(4\psi)] \tag{6}$$

259 where the intensity $I_{\lambda,0} = \eta_\lambda P_\lambda/(4d^2)$, while coefficients a_λ and b_λ are equal to $a_\lambda = F_{11,\lambda} + F_{22,\lambda}$ and $b_\lambda = 3F_{22,\lambda} - F_{11,\lambda}$.

260 Hence, $F_{22,\lambda}/F_{11,\lambda} = (1 + b_\lambda/a_\lambda)/(3 - b_\lambda/a_\lambda)$ so that the ratio $F_{22,\lambda}/F_{11,\lambda}$ at π −angle can be determined from the ratio

261 b_λ/a_λ . This ratio can be obtained from measurements of $I_\lambda(\psi)$, for different ψ-angles of the QWP, then adjusting these

262 variations with Eq. (6) to get accurate determinations of $I_{\lambda,0}a_\lambda$ and $I_{\lambda,0}b_\lambda$, then b_λ/a_λ. Evaluations of the dust lidar PDR are

263 then finally retrieved from Eq. (4):

$$PDR_\lambda = (1 - b_\lambda/a_\lambda)/2 \tag{7}$$

267 Within our methodology, the dust lidar PDR is independent of $I_{\lambda,0}$. For that reason, in Section 4, the applied voltage to the UV

268 and VIS-photodetectors is adjusted to each dust SD and mineralogy to gain in accuracy in the retrieved dust lidar PDR by

269 improving the signal-to-noise ratio on I_λ. For example, Fig. 3 provides simulations of $I_\lambda(\psi)/I_{\lambda,0}$ for the three following dust

270 lidar PDR case studies : 33 % dust lidar PDR (in full lines, i.e. $F_{22,\lambda}/F_{11,\lambda} = 0.5$), 25 % dust lidar PDR (in dashed-lines, i.e.

271 $F_{22,\lambda}/F_{11,\lambda} = 0.6$), 10 % dust lidar PDR (in dotted lines, i.e. $F_{22,\lambda}/F_{11,\lambda} = 0.82$). The curve minima, which are equal to

272 $I_{\lambda,m}/I_{\lambda,0} = a_\lambda - b_\lambda = F_{11,\lambda} - F_{22,\lambda}$, are shape-dependent : each curve hence exhibits non-vanishing minima since mineral dust

273 particles are nonspherical. Likewise, the curve maxima are equal to $I_{\lambda,M}/I_{\lambda,0} = a_\lambda + b_\lambda = 2F_{22,\lambda}$ and are size-dependent,

274 though it is also shape dependent. The dust lidar PDR is determined from $I_{\lambda,m}$ and $I_{\lambda,M}$ since, following Eq. (7),

275 $PDR_\lambda = I_{\lambda,m}/(I_{\lambda,m} + I_{\lambda,M})$, independently of $I_{\lambda,0}$.

276
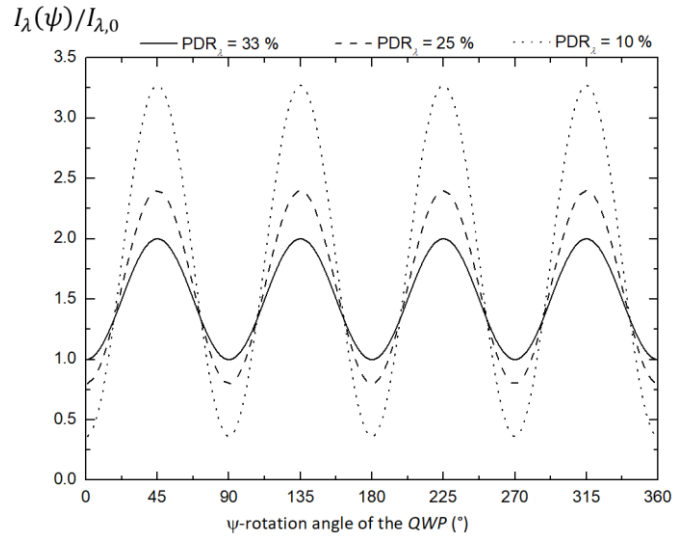
Figure 3: Numerical simulation of the dust backscattered light intensity $I_\lambda(\psi)/I_{\lambda,0}$ as a function of the orientation ψ of the QWP at a given wavelength at the three following case studies: $PDR_\lambda = 33\%$ (in full lines, corresponding to $F_{22,\lambda}/F_{11,\lambda} = 0.50$), : $PDR_\lambda = 25\%$ (in dashed-lines, $F_{22,\lambda}/F_{11,\lambda} = 0.60$), : $PDR_\lambda = 10\%$ (in dotted lines, $F_{22,\lambda}/F_{11,\lambda} = 0.82$).

3.5 Accuracy on the retrieved laboratory mineral dust lidar PDR

Special care has been taken to quantify the uncertainties on the retrieved dust lidar PDR. The systematic errors in the π-polarimeter are that encountered in 2λ-polarization lidar experiments, which we extensively studied (David et al., 2012) and can also be found in polarization lidar reference papers (Freudenthaler, 2016). To summarize, systematic errors arise from:

- *Imperfect definition of the polarization state of the incident radiation.* In the π–polarimeter, the polarization state of the electromagnetic radiation emitted from the laser is precisely set to $[1,1,0,0]^T$ (i.e. with no remaining ellipticity) by using two successive PBC.

- *Polarization cross-talk between the emitter and the detector polarization axes.* Likewise, on the detector side, to account for the imperfections of the retro-reflecting PBC ($R_s > 99.5\%, T_p > 90\%$), a secondary PBC is inserted between the retro-reflecting PBC and the light detector to ensure polarization cross-talk or undesired fraction R_pT_s originating from the p-component of the backscattered radiation are fully negligible. Hence, the π–polarimeter is sensitive to the s-component of the backscattered radiation only. Also, the emitting PBC being used as retro-reflecting PBC, any possible mismatch between the s-polarization axis of the emitted and detected backscattered radiations cannot occur.

- *Spectral cross-talk between the UV and the VIS-backscattered radiations.* Likewise, wavelength cross-talk is minimized by using selective interference filters exhibiting a higher than 5 optical density, at 355 nm wavelength in the VIS π–polarimeter and at 532 nm wavelength in the UV π–polarimeter.

297   •   *Multiple scattering can induce further light depolarization.* However, the single-scattering approximation is ensured
298   in our laboratory backscattering experiment (Mishchenko et al., 2007) where the particles are moving in a thin (2.5
299   mm) wide beam so that the volume element is optically thin in contrary to atmospheric chambers (1100 cm^{-3} for the
300   coarser SD).

301

302 Finally, to account for potential fluctuations in the dust particle number concentration that may cause variations in the dust

303 backscattered light intensity I_λ, a normalization channel has been added to the π-polarimeter by including a polarization-

304 insensitive light detector operating at scattering angle $\theta_0 = 165°$. The corresponding scattered light intensity $I_\lambda(\theta_0)$ is

305 quantified similarly to Eq. 5 considering a scattering angle of $\theta_0 : I_\lambda(\theta_0) = [1,0,0,0]^T[\mathbf{F}_\lambda(\theta_0)][\mathbf{QWP}(\psi)][\mathbf{PBC}][1,1,0,0]^T$,

306 where $[\mathbf{F}_\lambda(\theta_0)]$ is the scattering matrix at angle θ_0. There, the QWP and the PBC only act on the detector side while

307 (St_i) equals $[1,1,0,0]^T$. Hence, $I_\lambda(\theta_0) = I_{\lambda,0} \times [2F_{11,\lambda}(\theta_0) + F_{12,\lambda}(\theta_0) + F_{12,\lambda}(\theta_0)\cos(4\psi)]$. Once the variations of $I_\lambda(\theta_0)$

308 with ψ-angle are recorded, the $\cos(4\psi)$-dependency of $I_\lambda(\theta_0)$ can be removed by applying a numerical low-pass filter on

309 $I_\lambda(\theta_0)$, to get a light intensity proportional to the dust particles number concentration. As a result, in the light backscattering

310 curves presented in Section 4, the plotted quantity is the normalized backscattered light intensity $I_{\lambda,N} = I_\lambda(\pi)/I_\lambda(\theta_0)$, which

311 is insensitive to potential fluctuations in the dust particles number concentration. The scattered light intensities $I_\lambda(\pi)$ and

312 $I_\lambda(\theta_0)$ being correlated, the standard deviation σ_N on $I_{\lambda,N}$ was calculated by considering the covariance $\sigma_{I_\lambda I_\lambda(\theta_0)}$ of I_λ and

313 $I_\lambda(\theta_0)$. This covariance contributes to the uncertainty on $I_{\lambda,N}$ at a rate $-2I_\lambda \sigma_{I_\lambda I_\lambda(\theta_0)}/I_\lambda^3(\theta_0)$. Moreover, to gain in accuracy in

314 the dust lidar PDR retrievals, $I_{\lambda,N}$ was measured for a complete ψ-angle rotation, while averaging the acquired backscattered

315 light intensity over several thousand laser shots per ψ-angle, with resulting mean and standard deviations on $I_{\lambda,N}$ as plotted in

316 Fig. 4 and 5.

317 **4. Results and discussion**

318   In this section, using the methodology presented in Section 3, the lidar PDR of Arizona dust, Asian dust, silica and hematite

319 is evaluated and discussed at 355 and 532 nm wavelength for the finer and the coarser SD.

320 **4.1 Laboratory evaluation of the lidar PDR of Arizona and Asian dust**

321   Figure 4 displays the variations of $I_{\lambda,N}$ for Arizona (Fig. 4a) and Asian dust (Fig. 4b) as a function of the ψ-rotation angle

322 of the QWP for the finer (left panels) and the coarser SD (right panels) at 355 and 532 nm wavelength. The observed variations

323 are related to a determined size and shape distribution of the dust sample: indeed, as explained in Section 3.4, if the size (resp.

324 the shape) of the dust sample was varying during our acquisitions, the maxima (resp. the minima) of the curves would not

325 remain constant. As a result, the observed variations of $I_{\lambda,N}$ reveal the spectral and polarimetric backscattering characteristics

326 of each considered dust sample. Therefore, the experimental data points could be fitted with Eq. (6) to evaluate $F_{22,\lambda}/F_{11,\lambda}$

327 then the dust lidar *PDR* by applying Eq. (7). Table 1 presents the retrieved values of $F_{22,\lambda}/F_{11,\lambda}$ and of dust lidar *PDR*. The

328 uncertainty on $F_{22,\lambda}/F_{11,\lambda}$ results from the measurement errors of the laboratory π-polarimeter and leads to accurate evaluations

329 of the dust lidar *PDR*. Within experimental error bars, the lidar *PDR* of Arizona and Asian dust clearly differ, whatever the

330 chosen wavelength. The generally admitted value of around 33 % for the dust lidar *PDR* (Tesche et al., 2009) is only obtained

331 for Arizona dust: Asian dust exhibits a lower *PDR* in the range from 24 to 28 % depending on the considered *SD* and

332 wavelength. This suggests that the dust lidar *PDR* is primarily governed by the dust mineralogy and hence particles refractive

333 index. The sensitivity of the dust lidar *PDR* with the considered *SD* is indeed less pronounced: from the coarser to the finer

334 *SD*, a reduction in the dust lidar *PDR* of below 5 % is observed at 532 nm wavelength. At 355 nm wavelength however, the

335 Arizona and Asian dust lidar *PDR* seem practically insensitive to variations in the considered *SD*.
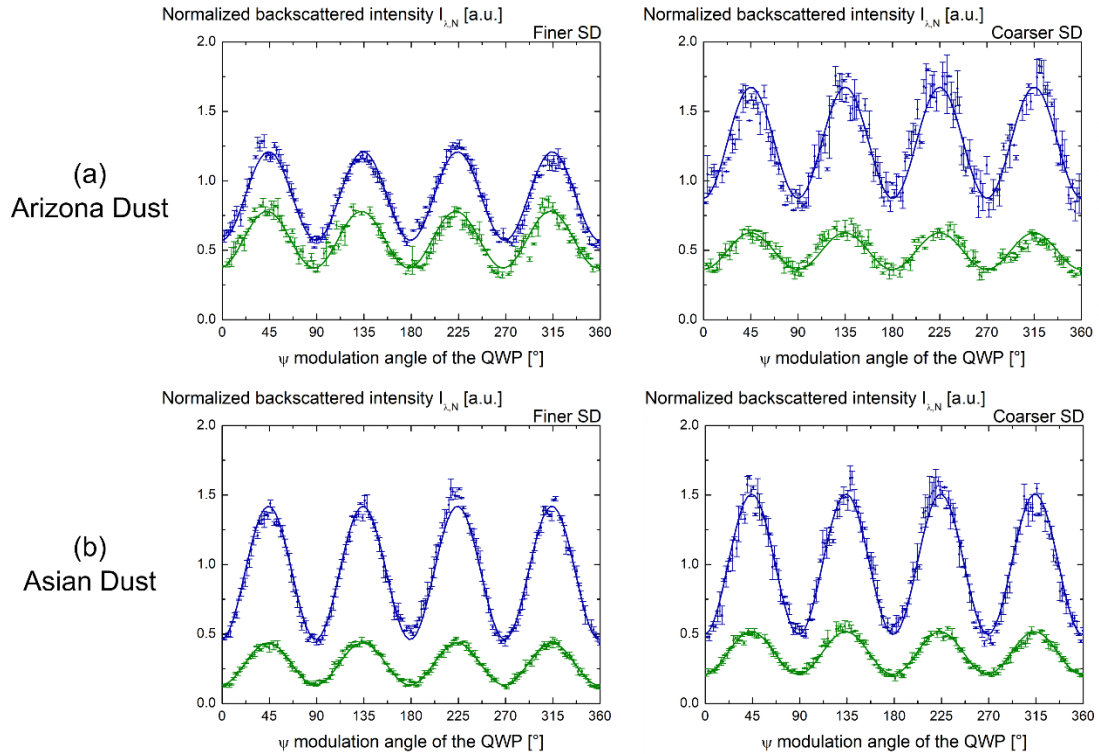
336

337 Figure 4: Normalized backscattered light intensity $I_{\lambda,N} = I_\lambda(\pi)/I_\lambda(\theta_0)$ of Arizona (a) and Asian dust (b) for finer $\boldsymbol{SD}$ (left panels) and

338 coarser $\boldsymbol{SD}$ (right panels), using the laboratory $\boldsymbol{\pi}$-polarimeter at lidar exact backscattering angle ($\boldsymbol{\theta = \pi}$) at 355 (blue) and 532 (green) nm.

339 The experimental data points are fitted with Eq. 6 to derive $\boldsymbol{F_{22,\lambda}/F_{11,\lambda}}$ and then the dust lidar $\boldsymbol{PDR}$ is derived using Eq. 7. Care should be

340 taken when comparing $\boldsymbol{I_{\lambda,N}}$ for Arizona and Asian dust since the applied voltage to the UV and VIS-photodetectors was adjusted to increase

341 the signal-to-noise ratio, as explained in Section 3.4. The Arizona dust lidar $\boldsymbol{PDR}$, retrieved from $\mathbf{I_{\lambda,m}/(I_{\lambda,m} + I_{\lambda,M})}$, is higher than that of

342 Asian dust.

343

344 Tab. 1: Laboratory measurement of the *PDR* of Arizona and Asian dust at 355 (blue) and 532 nm (green), for the finer and the coarser *SD*.

345 The *PDR* is calculated with Eq. 7 after the derivation of $F_{22,\lambda}/F_{11,\lambda}$ using the laboratory π-polarimeter presented in Section 3.2. The

346 uncertainty on $F_{22,\lambda}/F_{11,\lambda}$ is deduced from the evaluation of b_λ/a_λ, itself deduced from the least-square fit adjustment of I_λ. The uncertainty
347 on $F_{22,\lambda}/F_{11,\lambda}$ is mostly dominated by statistical uncertainties since our biases are minimized, as explained in Section 3.5.
348

Mineralogy	λ	Finer SD		Coarser SD	
	(nm)	$F_{22,\lambda}/F_{11,\lambda}$	PDR_λ (%)	$F_{22,\lambda}/F_{11,\lambda}$	PDR_λ (%)
Arizona dust	355	0.514 ± 0.007	$\mathbf{32.1 \pm 0.6}$	0.489 ± 0.012	$\mathbf{34.3 \pm 1.0}$
	532	0.512 ± 0.012	$\mathbf{32.3 \pm 1.0}$	0.464 ± 0.012	$\mathbf{36.6 \pm 1.1}$
Asian dust	355	0.603 ± 0.009	$\mathbf{24.7 \pm 0.6}$	0.603 ± 0.011	$\mathbf{24.8 \pm 0.8}$
	532	0.622 ± 0.009	$\mathbf{23.3 \pm 0.7}$	0.558 ± 0.011	$\mathbf{28.4 \pm 0.8}$

349

4.2 Laboratory evaluation of the lidar PDR of silica and hematite

351   By applying the same methodology, we obtain the PDR of silica and hematite, as presented in Fig. 5 and Table 2.
352 Accordingly, Fig. 5 is the analog of Fig. 4 for silica (Fig. 5a) and hematite (Fig. 5b). As for Arizona and Asian dust samples,
353 the lidar PDR of silica and hematite primarily depends on the particles CRI, at least at 355 nm wavelength where the silica
354 lidar PDR ranges from 23 to 33 % depending on the considered SD while the hematite lidar PDR reaches 10 % only. The silica
355 lidar PDR also strongly depends on the particles diameter: from the coarser to the finer SD, the silica dust lidar PDR reduces
356 by 10 % at both wavelengths. The dependence of the hematite dust lidar PDR with the SD is less pronounced, especially at
357 355 nm wavelength. The silica and hematite lidar PDR also strongly depend on the chosen lidar wavelength, with higher
358 depolarization observed at 355 nm wavelength for silica and at 532 nm wavelength for hematite.
359
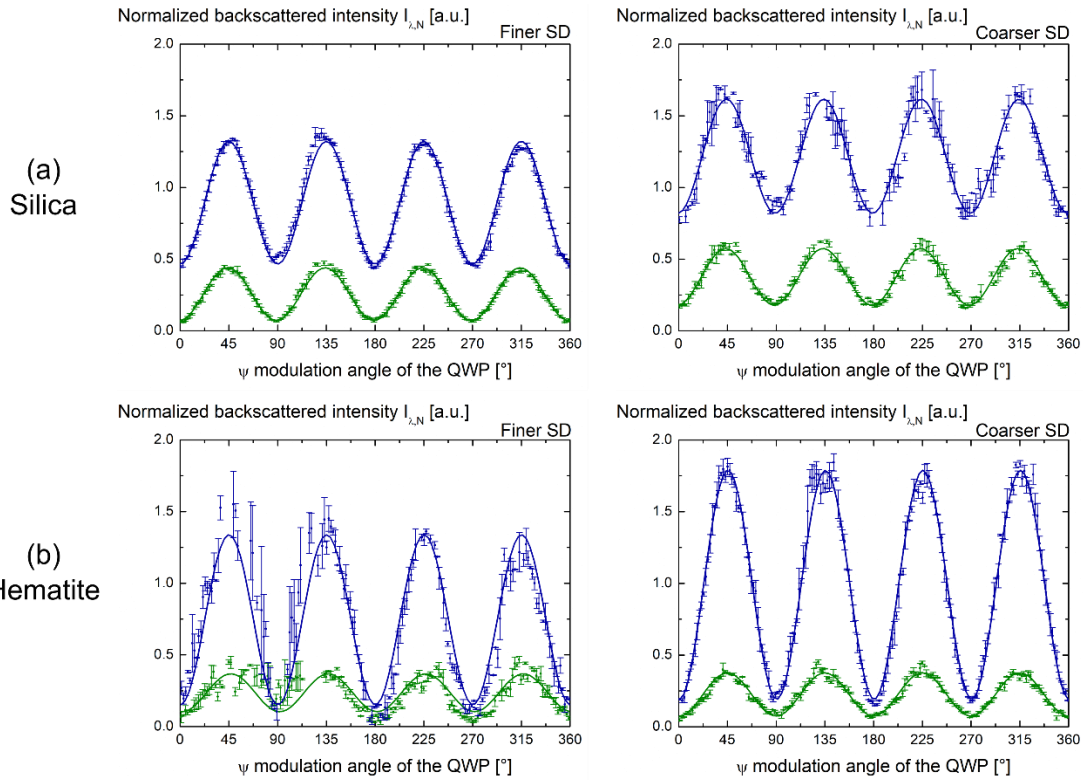
360

361 Figure 5: Same as Fig. 4 for silica (a-plots) and for hematite samples (b-plots).

362
363 Tab. 2: Same as Table 1 for silica and hematite.
364

Mineralogy	λ	Finer SD		Coarser SD	
	(nm)	$F_{22,\lambda}/F_{11,\lambda}$	PDR_λ (%)	$F_{22,\lambda}/F_{11,\lambda}$	PDR_λ (%)
Silica	355	0.622 ± 0.014	$\mathbf{23.3 \pm 0.9}$	0.506 ± 0.011	$\mathbf{32.8 \pm 1.0}$
	532	0.751 ± 0.016	$\mathbf{14.2 \pm 0.9}$	0.618 ± 0.016	$\mathbf{23.6 \pm 1.1}$
Hematite	355	0.805 ± 0.050	$\mathbf{10.8 \pm 2.5}$	0.823 ± 0.015	$\mathbf{9.7 \pm 0.7}$
	532	0.652 ± 0.055	$\mathbf{21.1 \pm 3.5}$	0.715 ± 0.019	$\mathbf{16.6 \pm 1.1}$

365

366 **4.3 Discussion**

367   Comparing our laboratory findings with other laboratory experiments is not straightforward, since as explained in the
368 introduction, none operates at 180.0° lidar exact backscattering angle, while the dust lidar PDR differs from near to exact
369 backscattering angles, especially when light absorbents are present (Cholleton et al., 2022). Moreover, the PDR is wavelength-
370 dependent and the size distributions (SD) used are different from other studies. Lidar field experiments provide accurate values

of the lidar PDR after accurate calibration procedure based on the scattering matrix (Freudenthaler, 2016; Belegante et al., 2018; Miffre et al., 2019). Although in such lidar field experiments, the measured PDR is usually that of dust mixtures (Miffre et al., 2011), the comparison with our laboratory findings remains interesting. In lidar retrievals (see for example (Tesche et al., 2009)), a dust lidar PDR of 30 % is often used. The laboratory π-polarimeter verifies this statement by providing the silica PDR, which is the main oxide present in mineral dust, equal to (33 ± 1) % for the coarser SD at 355 nm. In comparison, within our experimental error bars, the hematite lidar PDR, equal to (10 ± 1) %, is clearly lower. The real part n and the imaginary part κ of the hematite CRI, which are large compared with that of other chemical oxides present in mineral dust (see Section 2.1), can be responsible for the observed difference in the silica and hematite lidar PDR. Indeed, n and part κ modify the backscattering matrix elements, so does the corresponding dust lidar PDR. To highlight the role of κ on the hematite lidar PDR, the lidar PDR of rutile was measured with our π-polarimeter. Indeed, the real part of the rutile CRI is as large as that of hematite but its imaginary part is negligible compared with that of hematite. As a result, the rutile lidar PDR substantially differed from that of hematite, showing the key role played by light absorption in the measured hematite lidar PDR. In turn, Arizona dust exhibits a higher PDR than Asian dust, due to the higher proportion in hematite in the latter. Hence and as a conclusion, our laboratory findings show that, when the light absorbent hematite is present, it mainly governs the dust lidar PDR, which hence primarily depends on the particles mineralogy, with less pronounced variations with the particles size and wavelength. This finding is in line with (Kahnert, 2015; Kahnert et al., 2020) numerical findings, who highlighted that the dust PDR is strongly modulated by the particles inhomogeneity, especially in the lidar backward scattering direction and in the presence of hematite. We here quantify this effect with a laboratory experiment that accounts for the real shape of mineral dust. The shape dependence of the hematite PDR is weak due to its large imaginary part of complex refractive index: following Wiscombe and Mugnai (1986) or Mishchenko et al. (1997), the effect of particle shape becomes weaker with increasing imaginary part of the refractive index, a conclusion also drawn by Meland et al. (2011). In contrast, when the proportion of hematite becomes negligible, as is the case for silica and Arizona dust, our laboratory findings show that the dust lidar PDR then increases with increasing the particles size, though the shape dependence may then also play a role. Also, it would be interesting to investigate giant dust particles (Ryder et al., 2019). Likewise, in the literature (Sakai et al., 2010; Hofer et al., 2020; Järvinen et al., 2016; Mamouri and Ansmann, 2017), the dust lidar PDR is usually found to increase with the particles size from the fine to the coarse mode of the SD. The (355, 532) nm wavelength dependence of the dust lidar PDR then becomes key for discussing on the involved particle sizes, thus underlying the importance of dual-wavelength (or more) polarization lidar instruments. We here establish this result in laboratory at 180.0° and (355, 532) nm wavelength, and moreover, show that this consideration holds only when hematite, which is a strong light absorbent, is not involved : the hematite lidar PDR is indeed higher in the finer mode of the SD.

To go further and discuss on the role of light absorption in the retrieved dust lidar PDR, we here propose a basic partitioning model in which the dust particles mixture $(d) = \{Abs, \overline{Abs}\}$ is comprised of two components: an absorbing component (Abs),

404 mainly corresponding to hematite particles, and a non-absorbing component ($\overline{Abs}$), mainly corresponding to silica-particles.

405 For simplicity, we here resume the absorbing (resp. non-absorbing) component to hematite (resp. silica)-particles with

406 respective abbreviations (Hmt) and (Sil). We focus on the 355 nm wavelength at which hematite is an efficient light absorber

407 and on the coarser SD as the dependence of the dust lidar PDR with size is less pronounced than with the particles mineralogy.

408 In Appendix A is detailed the derivation of the lidar PDR of such a dust-particles mixture $(d) = \{Hmt, Sil\}$ (hereafter noted

409 δ_d, as in lidar applications). This Appendix is an extension of our previous works (Miffre et al., 2011; David et al., 2013, 2014;

410 Mehri et al., 2018) for the case study where both components $\{Hmt, Sil\}$ are nonspherical. The lidar PDR of such a dust-

411 particles mixture relates to that of its pure components (hereafter noted δ_{Sil} and δ_{Hmt}) as follows:

412

413 $$\delta_d = \frac{-e + (c + e)X_{\text{Hmt}}}{f - (d + f)X_{\text{Hmt}}} \tag{8}$$

414

415 where the expressions of the c, d, e and f-coefficients are provided in Appendix A and independently on the depolarization

416 ratios δ_{Sil} and δ_{Hmt} of silica and iron oxides. X_{Hmt} is the fraction of Hmt to dust particles backscattering. Following Eq. (8)

417 and Appendix A, Fig. 6 displays the variation of δ_d as a function of X_{Hmt} when considering δ_{Sil} = 33 % and δ_{Hmt} = 10 %, as

418 obtained in our laboratory findings at 355 nm wavelength with the coarser SD. As shown in Fig. 6, the dust lidar PDR lies in

419 between δ_{Sil} and δ_{Hmt} and equals δ_{Sil} (resp. δ_{Hmt}) only when X_{Hmt} = 0 (resp. 1), depending on the fraction X_{Hmt} of light

420 corresponding to the absorbent of the dust particle mixture. Hence, Arizona dust, which contains a lower fraction of hematite,

421 exhibits a higher lidar PDR compared with Asian dust, at least at 355 nm wavelength where hematite is strongly absorbing.

422 Though rather simple, our model interestingly highlights the key role played by light absorption in the retrieved Asian dust

423 lidar PDR. To go further and provide a quantitative analysis, this simple model should be refined, by considering also the other

424 chemical oxides present in mineral dust, other lidar wavelengths, as well as other SD and the effect of shape. To handle such

425 a complex issue, more laboratory experiments are required on other chemical oxides, ideally also at 1064 nm wavelength. This

426 work is however beyond the scope of this paper. Still as is, our model provides an interpretation of the laboratory-observed

427 differences in the dust lidar PDR when the light absorbent hematite is involved. In the most general case, the dust lidar PDR

428 hence appears as a complex function of the particles mineralogy, SD, wavelength and shape. Comparison with lidar field

429 experiments, involving particle mixtures, with a more complex distribution of sizes and refractive indices, is then not

430 straightforward, as underscored by comparison with Hu et al. (2020) who reported 0.28 - 0.32 ± 0.07 at 355 nm wavelength.

431 Though this complex dependence is difficult to disentangle, our laboratory findings show that the dust lidar PDR is primarily

432 affected by the particles mineralogy, at least when hematite is involved.

433

434
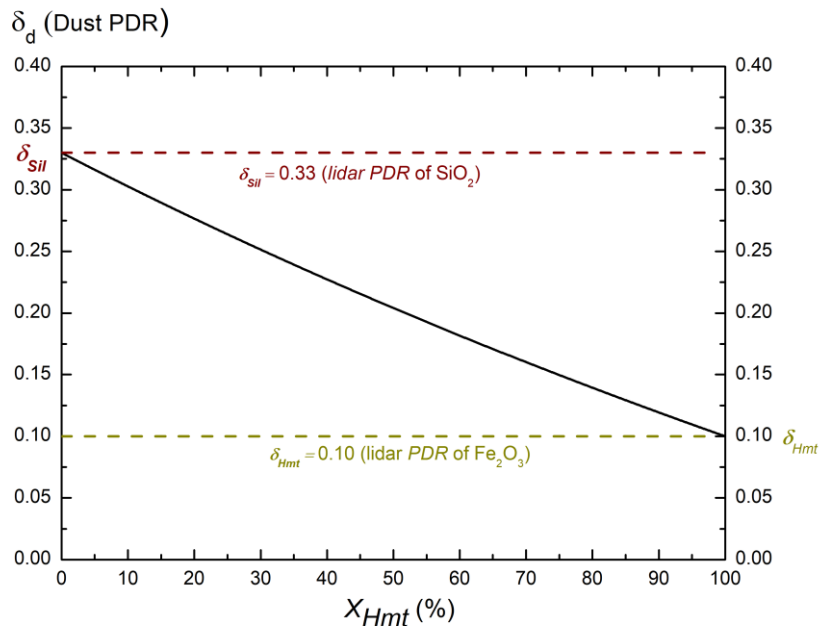
Figure 6: Numerical simulation of the 355 nm Lidar PDR of a two-component particles mixture $(d) = \{Hmt, Sil\}$, composed of hematite (Hmt) and silica (Sil) oxides as a function of the $X_{Hmt} = \beta_{Hmt}/\beta_d$ fraction of Hmt to d-particles backscattering, following Eq. (8) and Appendix A, by accounting for our laboratory experimental findings for $\delta_{Sil} = 33$ % and $\delta_{Hmt} = 10$ % (see Table 2 at 355 nm wavelength with coarser SD).

5 Summary and conclusion

In this paper, the dependence of the lidar particles depolarization ratio (PDR) of pure mineral dust with complex refractive index (CRI) and size is for the first time investigated through a laboratory π-polarimeter operating at 180.0° lidar backscattering angle and (355, 532) nm wavelengths for lidar purposes. The goal of this work is to improve the knowledge on the dust lidar PDR, which is an important input parameter involved in lidar partitioning algorithms, which are widely applied to reveal the contribution of mineral dust in particles external mixtures (Tesche et al., 2009; Mehri et al., 2018). While mineral dust exhibits a complex and highly irregular shape, which is difficult to model mathematically and numerically, our laboratory approach allows accounting for the real shape of mineral dust. Our laboratory π-polarimeter is likewise a good complement to lidar field experiments, which provide accurate retrievals of the lidar PDR of particles mixtures involving mineral dust. Another advantage of our laboratory π-polarimeter lies in its ability to provide accurate retrievals of the lidar PDR of pure mineral dust samples, differing in CRI and size. The π-polarimeter indeed operates at 180.0° lidar backscattering angle and at (355, 532) nm lidar wavelengths: no assumption is made to retrieve the dust lidar PDR. This is a key novelty of our study. Indeed, the variation of the dust lidar PDR with scattering angle and wavelength cannot be analytically calculated (Bohren and Huffman, 1983; Mishchenko et al., 2002) for complex-shaped particles such as mineral dust. Hence, our π-polarimeter

453 improves the knowledge on the dust PDR, provided in the literature at non 180.0° backscattering angle and / or at wavelengths

454 differing from (355, 532 nm). Our work provides sixteen accurate dust lidar PDR-values, corresponding to four different

455 complex refractive indices, studied at two size distributions (fine, coarse) and at (355, 532) nm wavelengths (see Section 4).

456 The precision on the retrieved dust PDR from the laboratory π-polarimeter is detailed in Section 3. To investigate the

457 dependence of the dust lidar PDR with CRI, hematite, the main light absorbent present in mineral dust, was considered in

458 addition to silica oxide, the main chemical oxide present in mineral dust, which is practically nonabsorbent. At 355 nm, our

459 laboratory π-polarimeter provides values of the PDR of coarser silica of (33 ± 1) % while that of coarser hematite is only

460 (10 ± 1) %. In Section 4, this large difference is explained by accounting for the high imaginary part of the hematite CRI. In

461 turn, Arizona dust exhibits a higher depolarization ratio than Asian dust, due to the higher proportion in hematite in the latter.

462 As a result, when the strong light absorbent hematite is involved, the dust lidar PDR is primarily governed by the particles

463 mineralogy and the variations of the dust lidar PDR with size are less pronounced. The dependence of the PLDR on the

464 particles shape is not pronounced in our experiment where hematite, which exhibits a large imaginary part of complex

465 refractive index, plays a key role (Wiscombe and Mugnai, 1986, Mishchenko et al., 1997, Meland et al., 2011). When hematite

466 is less or not involved, the dust lidar PDR increases with increasing sizes and the (355, 532) nm wavelength dependence of

467 the dust lidar PDR then becomes key for discussing on the involved particle sizes, thus underscoring the importance of dual

468 wavelengths (or more) polarization lidar instruments. To further disentangle the complex dependence of the dust lidar PDR

469 with complex refractive index and size, our methodology should be extended to other chemical oxides, other natural mineral

470 dust samples, other SD and other wavelengths, as well as other shape distributions. Giant dust particles, whose importance has

471 been highlighted by Ryder et al. (2019), would likewise be interesting to study specifically. This is however far beyond the

472 scope of this paper : we here focused on (355, 532) nm wavelengths, since mineral dust slightly absorb light in the near infra-

473 red (Di Biagio et al., 2019). Still, the above laboratory findings underscore the importance of accounting for the wavelength

474 dependence of the dust lidar PDR, whatever the hematite proportion. The spectral dependence of the dust lidar PDR is indeed

475 instructive (Burton et al., 2016; Haarig et al., 2022; Miffre et al., 2020). Outlooks of this work are obviously also interesting,

476 as underscored by recent papers (Kahnert et al., 2020; Luo et al., 2022), discussing on the ability of the spheroidal model to

477 mimic light scattering by complex-shaped mineral dust.

478 **Appendix A**

479 The goal of this Appendix is to establish the expression of the lidar PDR of a two-component particle mixture $(p) =$

480 $\{ns_1, ns_2\}$ composed of two non-spherical components ns_1 and ns_2. As in lidar applications, the lidar PDR of p, ns_1 and ns_2-

481 particles are respectively noted δ_p, δ_{ns_1} and δ_{ns_2}. The starting point is given by the set of four equations:

482

483 $\beta_{p,//} = \beta_{ns_1,//} + \beta_{ns_2,//}$ (A-1-a)

484    $\beta_{p,\perp} = \beta_{ns_1,\perp} + \beta_{ns_2,\perp}$ (A-1-b)

485    $\delta_{ns_1} = \beta_{ns_1,\perp}/\beta_{ns_1,//}$ (A-1-c)

486    $\delta_{ns_2} = \beta_{ns_2,\perp}/\beta_{ns_2,//}$ (A-1-d)

487

488   where $\beta_{p,//}$ and $\beta_{p,\perp}$ are the lidar particles backscattering coefficients, evaluated from a polarization lidar experiment carried

489   out at wavelength λ (here omitted to ease the reading). The backscattering coefficient β_{ns_1} of ns_1-particles is then retrieved by

490   noting that $\beta_{ns_1} = \beta_{ns_1,//} + \beta_{ns_1,\perp} = \beta_{ns1,\perp}(1 + 1/\delta_{ns_1})$ (Miffre et al., 2011; David et al., 2013). Moreover, $\beta_{ns_1,\perp}$ can be

491   expressed as a fonction of $\beta_{p,//}$ and $\beta_{p,\perp}$ since $\beta_{ns_1,\perp} = \beta_{p,\perp} - \beta_{ns_2,\perp} = \beta_{p,\perp} - \delta_{ns_2}\beta_{ns_2,//} = \beta_{p,\perp} - \delta_{ns_2}(\beta_{p,//} - \beta_{ns_1,\perp}/\delta_{ns_1})$

492   using Eqs. (A-1). Hence, $\beta_{ns_1,\perp} = (\beta_{p,\perp} - \delta_{ns_2}\beta_{p,//})/(1 - \delta_{ns_2}/\delta_{ns_1})$. By applying the same methodology to ns_2- particles,

493   we finally get:

494

495    $$\begin{pmatrix} \beta_{ns_1} \\ \beta_{ns_2} \end{pmatrix} = \begin{bmatrix} c & d \\ e & f \end{bmatrix} \begin{pmatrix} \beta_{p,//} \\ \beta_{p,\perp} \end{pmatrix}$$ (A-2)

496

497   where the c, d, e and f-coefficients only depend on the depolarization ratios δ_{ns_1} and δ_{ns_2} :

498

499    $c = -\delta_{ns_2}(1 + 1/\delta_{ns_1})/(1 - \delta_{ns_2}/\delta_{ns_1})$ (A-3-a)

500    $d = (1 + 1/\delta_{ns_1})/(1 - \delta_{ns_2}/\delta_{ns_1})$ (A-3-b)

501    $e = -\delta_{ns_1}(1 + 1/\delta_{ns_2})/(1 - \delta_{ns_1}/\delta_{ns_2})$ (A-3-c)

502    $f = (1 + 1/\delta_{ns_2})/(1 - \delta_{ns_1}/\delta_{ns_2})$ (A-3-d)

503

504   The 2 x 2 matrix introduced in Eq. (A-2) can be inverted to get the expression of $\beta_{p,//}$ and $\beta_{p,\perp}$ and hence $\delta_p = \beta_{p,\perp}/\beta_{p,//}$. By

505   introducing $X_{ns2} = \beta_{ns2}/(\beta_{ns1} + \beta_{ns2})$ the fraction of ns_2 to p-particles backscattering, we finally get the relationship

506   between δ_p and δ_{ns1} and δ_{ns2} :

507

508    $$\delta_p = \frac{-e + (c + e)X_{ns2}}{f - (d + f)X_{ns2}}$$ $(A - 4)$

509

510   In the specific case where ns_2-particles are spherical (i.e. $\delta_{ns_2} = 0$), the expressions of the c, d, e and f-coefficients simplify

511   and the relationship between δ_p and $X_{ns2} = X_{ns}$ becomes identical to that we already published in (Miffre et al., 2011; David

512   et al., 2013). This new material is hence as an extension of our previous works (Miffre et al., 2011; David et al., 2013, 2014;

513   Mehri et al., 2018) to the case study where both components of the particles mixture $(p) = \{ns_1, ns_2\}$ are nonspherical.

514

Author contribution

Alain Miffre: Conceptualization, Formal analysis, Investigation, Methodology, Supervision, Writing - original draft, Writing - review & editing **Danaël Cholleton**: Formal analysis, Investigation, Software, Visualization, Writing - review & editing. **Clément Noël**: Software, Writing - review & editing **Patrick Rairoux**: Project administration, Supervision, Writing - review & editing.

Competing interests

The authors declare that they have no conflict of interest.

Acknowledgements

The French National Center for Space Studies (CNES) is acknowledged for financial support.

References

Belegante, L., Bravo-Aranda, J. A., Freudenthaler, V., Nicolae, D., Nemuc, A., Ene, D., Alados-Arboledas, L., Amodeo, A., Pappalardo, G., D'Amico, G., Amato, F., Engelmann, R., Baars, H., Wandinger, U., Papayannis, A., Kokkalis, P., and Pereira, S. N.: Experimental techniques for the calibration of lidar depolarization channels in EARLINET, Atmospheric Meas. Tech., 11, 1119–1141, https://doi.org/10.5194/amt-11-1119-2018, 2018.

Bohren, C. F. and Huffman, D. R.: Absorption and scattering of light by small particles, Wiley-VCH, Weinheim, 530 pp., 1983.

Bristow, C. S., Hudson-Edwards, K. A., and Chappell, A.: Fertilizing the Amazon and equatorial Atlantic with West African dust: AFRICAN FERTILIZER FOR AMAZON AND ATLANTIC, Geophys. Res. Lett., 37, n/a-n/a, https://doi.org/10.1029/2010GL043486, 2010.

Bullard, J. E. and White, K.: Quantifying iron oxide coatings on dune sands using spectrometric measurements: An example from the Simpson-Strzelecki Desert, Australia, J. Geophys. Res. Solid Earth, 107, ECV 5-1-ECV 5-11, https://doi.org/10.1029/2001JB000454, 2002.

Burton, S. P., Ferrare, R. A., Hostetler, C. A., Hair, J. W., Rogers, R. R., Obland, M. D., Butler, C. F., Cook, A. L., Harper, D. B., and Froyd, K. D.: Aerosol classification using airborne High Spectral Resolution Lidar measurements – methodology and examples, Atmospheric Meas. Tech., 5, 73–98, https://doi.org/10.5194/amt-5-73-2012, 2012.

Burton, S. P., Chemyakin, E., Liu, X., Knobelspiesse, K., Stamnes, S., Sawamura, P., Moore, R. H., Hostetler, C. A., and Ferrare, R. A.: Information content and sensitity of the $3\,\beta + 2\,\alpha$ lidar measurement system for aerosol microphysical retrievals, Atmospheric Meas. Tech., 9, 5555–5574, https://doi.org/10.5194/amt-9-5555-2016, 2016.

543 Caponi, L., Formenti, P., Massabò, D., Di Biagio, C., Cazaunau, M., Pangui, E., Chevaillier, S., Landrot, G., Andreae, M. O.,
544 Kandler, K., Piketh, S., Saeed, T., Seibert, D., Williams, E., Balkanski, Y., Prati, P., and Doussin, J.-F.: Spectral- and size-
545 resolved mass absorption efficiency of mineral dust aerosols in the shortwave spectrum: a simulation chamber study,
546 Atmospheric Chem. Phys., 17, 7175–7191, https://doi.org/10.5194/acp-17-7175-2017, 2017.

547 Cholleton, D., Rairoux, P., and Miffre, A.: Laboratory Evaluation of the (355, 532) nm Particle Depolarization Ratio of Pure
548 Pollen at 180.0° Lidar Backscattering Angle, Remote Sens., 14, 3767, https://doi.org/10.3390/rs14153767, 2022.

549 David, G., Miffre, A., Thomas, B., and Rairoux, P.: Sensitive and accurate dual-wavelength UV-VIS polarization detector for
550 optical remote sensing of tropospheric aerosols, Appl. Phys. B, 108, 197–216, https://doi.org/10.1007/s00340-012-5066-x,
551 2012.

552 David, G., Thomas, B., Nousiainen, T., Miffre, A., and Rairoux, P.: Retrieving simulated volcanic, desert dust and sea-salt
553 particle properties from two/three-component particle mixtures using UV-VIS polarization lidar and T matrix, Atmospheric
554 Chem. Phys., 13, 6757–6776, https://doi.org/10.5194/acp-13-6757-2013, 2013.

555 David, G., Thomas, B., Dupart, Y., D'Anna, B., George, C., Miffre, A., and Rairoux, P.: UV polarization lidar for remote
556 sensing new particles formation in the atmosphere, Opt. Express, 22, A1009, https://doi.org/10.1364/OE.22.0A1009, 2014.

557 Di Biagio, C., Formenti, P., Balkanski, Y., Caponi, L., Cazaunau, M., Pangui, E., Journet, E., Nowak, S., Andreae, M. O.,
558 Kandler, K., Saeed, T., Piketh, S., Seibert, D., Williams, E., and Doussin, J.-F.: Complex refractive indices and single-
559 scattering albedo of global dust aerosols in the shortwave spectrum and relationship to size and iron content, Atmospheric
560 Chem. Phys., 19, 15503–15531, https://doi.org/10.5194/acp-19-15503-2019, 2019.

561 Dupart, Y., King, S. M., Nekat, B., Nowak, A., Wiedensohler, A., Herrmann, H., David, G., Thomas, B., Miffre, A., Rairoux,
562 P., D'Anna, B., and George, C.: Mineral dust photochemistry induces nucleation events in the presence of SO2, Proc. Natl.
563 Acad. Sci., 109, 20842–20847, https://doi.org/10.1073/pnas.1212297109, 2012.

564 Formenti, P., Caquineau, S., Chevaillier, S., Klaver, A., Desboeufs, K., Rajot, J. L., Belin, S., and Briois, V.: Dominance of
565 goethite over hematite in iron oxides of mineral dust from Western Africa: Quantitative partitioning by X-ray absorption
566 spectroscopy, J. Geophys. Res. Atmospheres, 119, 12,740-12,754, https://doi.org/10.1002/2014JD021668, 2014.

567 Francis, D., Nelli, N., Fonseca, R., Weston, M., Flamant, C., and Cherif, C.: The dust load and radiative impact associated
568 with the June 2020 historical Saharan dust storm, Atmos. Environ., 268, 118808,
569 https://doi.org/10.1016/j.atmosenv.2021.118808, 2022.

570 Freudenthaler, V.: About the effects of polarising optics on lidar signals and the Δ90 calibration, Atmospheric Meas.
571 Tech., 9, 4181–4255, https://doi.org/10.5194/amt-9-4181-2016, 2016.

572 Freudenthaler, V., Esselborn, M., Wiegner, M., Heese, B., Tesche, M., Ansmann, A., MüLLER, D., Althausen, D., Wirth, M.,
573 Fix, A., Ehret, G., Knippertz, P., Toledano, C., Gasteiger, J., Garhammer, M., and Seefeldner, M.: Depolarization ratio profiling
574 at several wavelengths in pure Saharan dust during SAMUM 2006, Tellus B Chem. Phys. Meteorol., 61, 165–179,
575 https://doi.org/10.1111/j.1600-0889.2008.00396.x, 2009.

576 Gasteiger, J., Wiegner, M., GROß, S., Freudenthaler, V., Toledano, C., Tesche, M., and Kandler, K.: Modelling lidar-relevant
577 optical properties of complex mineral dust aerosols, Tellus Ser. B Chem. Phys. Meteorol., 63, 725–741,
578 https://doi.org/10.1111/j.1600-0889.2011.00559.x, 2011.

579 Gautam, P., Maughan, J. B., Ilavsky, J., and Sorensen, C. M.: Light scattering study of highly absorptive, non-fractal, hematite
580 aggregates, J. Quant. Spectrosc. Radiat. Transf., 246, 106919, https://doi.org/10.1016/j.jqsrt.2020.106919, 2020.

Glen, A. and Brooks, S. D.: A new method for measuring optical scattering properties of atmospherically relevant dusts using the Cloud and Aerosol Spectrometer with Polarization (CASPOL), Atmospheric Chem. Phys., 13, 1345–1356, https://doi.org/10.5194/acp-13-1345-2013, 2013.

Go, S., Lyapustin, A., Schuster, G. L., Choi, M., Ginoux, P., Chin, M., Kalashnikova, O., Dubovik, O., Kim, J., da Silva, A., Holben, B., and Reid, J. S.: Inferring iron-oxide species content in atmospheric mineral dust from DSCOVR EPIC observations, Atmospheric Chem. Phys., 22, 1395–1423, https://doi.org/10.5194/acp-22-1395-2022, 2022.

Gómez Martín, J. C., Guirado, D., Frattin, E., Bermudez-Edo, M., Cariñanos Gonzalez, P., Olmo Reyes, F. J., Nousiainen, T., Gutiérrez, P. J., Moreno, F., and Muñoz, O.: On the application of scattering matrix measurements to detection and identification of major types of airborne aerosol particles: Volcanic ash, desert dust and pollen, J. Quant. Spectrosc. Radiat. Transf., 271, 107761, https://doi.org/10.1016/j.jqsrt.2021.107761, 2021.

Haarig, M., Ansmann, A., Engelmann, R., Baars, H., Toledano, C., Torres, B., Althausen, D., Radenz, M., and Wandinger, U.: First triple-wavelength lidar observations of depolarization and extinction-to-backscatter ratios of Saharan dust, Atmospheric Chem. Phys., 22, 355–369, https://doi.org/10.5194/acp-22-355-2022, 2022.

Hofer, J., Ansmann, A., Althausen, D., Engelmann, R., Baars, H., Fomba, K. W., Wandinger, U., Abdullaev, S. F., and Makhmudov, A. N.: Optical properties of Central Asian aerosol relevant for spaceborne lidar applications and aerosol typing at 355 and 532 nm, Atmospheric Chem. Phys., 20, 9265–9280, https://doi.org/10.5194/acp-20-9265-2020, 2020.

Hu, Q., Wang, H., Goloub, P., Li, Z., Veselovskii, I., Podvin, T., Li, K., and Korenskiy, M.: The characterization of Taklamakan dust properties using a multiwavelength Raman polarization lidar in Kashi, China, Atmospheric Chem. Phys., 20, 13817–13834, https://doi.org/10.5194/acp-20-13817-2020, 2020.

Huang, Y., Kok, J. F., Saito, M., and Muñoz, O.: Single-scattering properties of ellipsoidal dust aerosols constrained by measured dust shape distributions, Atmospheric Chem. Phys. Discuss., 1–23, https://doi.org/10.5194/acp-2022-633, 2022.

van de Hulst, H. C.: Light Scattering by Small Particles, Courier Corporation, 500 pp., 1957.

Iwai, T.: Polarization Analysis of Light Scattered by Pollen Grains of *Cryptomeria japonica*, Jpn. J. Appl. Phys., 52, 062404, https://doi.org/10.7567/JJAP.52.062404, 2013.

Järvinen, E., Kemppinen, O., Nousiainen, T., Kociok, T., Möhler, O., Leisner, T., and Schnaiter, M.: Laboratory investigations of mineral dust near-backscattering depolarization ratios, J. Quant. Spectrosc. Radiat. Transf., 178, 192–208, https://doi.org/10.1016/j.jqsrt.2016.02.003, 2016.

Kahnert, M.: Modelling radiometric properties of inhomogeneous mineral dust particles: Applicability and limitations of effective medium theories, J. Quant. Spectrosc. Radiat. Transf., 152, 16–27, https://doi.org/10.1016/j.jqsrt.2014.10.025, 2015.

Kahnert, M., Kanngießer, F., Järvinen, E., and Schnaiter, M.: Aerosol-optics model for the backscatter depolarisation ratio of mineral dust particles, J. Quant. Spectrosc. Radiat. Transf., 254, 107177, 2020.

Kandler, K., Lieke, K., Benker, N., Emmel, C., Küpper, M., Müller-Ebert, D., Ebert, M., Scheuvens, D., Schladitz, A., Schütz, L., and Weinbruch, S.: Electron microscopy of particles collected at Praia, Cape Verde, during the Saharan Mineral Dust Experiment: particle chemistry, shape, mixing state and complex refractive index, Tellus Ser. B Chem. Phys. Meteorol., 63, 475–496, https://doi.org/10.1111/j.1600-0889.2011.00550.x, 2011.

Kosmopoulos, P. G., Kazadzis, S., Taylor, M., Athanasopoulou, E., Speyer, O., Raptis, P. I., Marinou, E., Proestakis, E., Solomos, S., Gerasopoulos, E., Amiridis, V., Bais, A., and Kontoes, C.: Dust impact on surface solar irradiance assessed with

618 model simulations, satellite observations and ground-based measurements, Atmospheric Meas. Tech., 10, 2435–2453,
619 https://doi.org/10.5194/amt-10-2435-2017, 2017.

620 Lamb, K. D., Matsui, H., Katich, J. M., Perring, A. E., Spackman, J. R., Weinzierl, B., Dollner, M., and Schwarz, J. P.: Global-
621 scale constraints on light-absorbing anthropogenic iron oxide aerosols, Npj Clim. Atmospheric Sci., 4, 1–12, 2021.

622 Lindqvist, H., Jokinen, O., Kandler, K., Scheuvens, D., and Nousiainen, T.: Single scattering by realistic, inhomogeneous
623 mineral dust particles with stereogrammetric shapes, Atmospheric Chem. Phys., 14, 143–157, https://doi.org/10.5194/acp-14-
624 143-2014, 2014.

625 Liu, J., Zhang, Q., Huo, Y., Wang, J., and Zhang, Y.: An experimental study on light scattering matrices for Chinese loess dust
626 with different particle size distributions, Atmospheric Meas. Tech., 13, 4097–4109, https://doi.org/10.5194/amt-13-4097-2020,
627 2020.

628 Longtin, D. R., Shettle, E. P., Hummel, J. R., and Pryce, J. D.: A wind dependent desert aerosol model: Radiative properties,
629 OPTIMETRICS INC BURLINGTON MA, 1988.

630 Luo, J., Li, Z., Fan, C., Xu, H., Zhang, Y., Hou, W., Qie, L., Gu, H., Zhu, M., Li, Y., and Li, K.: The polarimetric characteristics
631 of dust with irregular shapes: evaluation of the spheroid model for single particles, Atmospheric Meas. Tech., 15, 2767–2789,
632 https://doi.org/10.5194/amt-15-2767-2022, 2022.

633 Mamouri, R.-E. and Ansmann, A.: Potential of polarization/Raman lidar to separate fine dust, coarse dust, maritime, and
634 anthropogenic aerosol profiles, Atmospheric Meas. Tech., 10, 3403–3427, https://doi.org/10.5194/amt-10-3403-2017, 2017.

635 Mehri, T., Kemppinen, O., David, G., Lindqvist, H., Tyynelä, J., Nousiainen, T., Rairoux, P., and Miffre, A.: Investigating the
636 size, shape and surface roughness dependence of polarization lidars with light-scattering computations on real mineral dust
637 particles: Application to dust particles' external mixtures and dust mass concentration retrievals, Atmospheric Res., 203, 44–
638 61, https://doi.org/10.1016/j.atmosres.2017.11.027, 2018.

639 Meland, B., Kleiber, P. D., Grassian, V. H., and Young, M. A.: Visible light scattering study at 470, 550, and 660nm of
640 components of mineral dust aerosol: Hematite and goethite, J. Quant. Spectrosc. Radiat. Transf., 112, 1108–1118,
641 https://doi.org/10.1016/j.jqsrt.2010.12.002, 2011.

642 Miffre, A., David, G., Thomas, B., and Rairoux, P.: Atmospheric non-spherical particles optical properties from UV-
643 polarization lidar and scattering matrix, Geophys. Res. Lett., 38, L16804, https://doi.org/10.1029/2011GL048310, 2011.

644 Miffre, A., Mehri, T., Francis, M., and Rairoux, P.: UV–VIS depolarization from Arizona Test Dust particles at exact
645 backscattering angle, J. Quant. Spectrosc. Radiat. Transf., 169, 79–90, https://doi.org/10.1016/j.jqsrt.2015.09.016, 2016.

646 Miffre, A., Cholleton, D., Mehri, T., and Rairoux, P.: Remote Sensing Observation of New Particle Formation Events with a
647 (UV, VIS) Polarization Lidar, Remote Sens., 11, 1761, https://doi.org/10.3390/rs11151761, 2019.

648 Miffre, A., Cholleton, D., and Rairoux, P.: On the use of light polarization to investigate the size, shape, and refractive index
649 dependence of backscattering Ångström exponents, Opt. Lett., 45, 1084–1087, https://doi.org/10.1364/OL.385107, 2020.

650 Mishchenko, M. I. and Travis, L. D.: Capabilities and limitations of a current FORTRAN implementation of the T-matrix
651 method for randomly oriented, rotationally symmetric scatterers, J. Quant. Spectrosc. Radiat. Transf., 60, 309–324,
652 https://doi.org/10.1016/S0022-4073(98)00008-9, 1998.

653   Mishchenko, M. I., Travis, L. D., Kahn, R. A., and West, R. A.: Modeling phase functions for dustlike tropospheric aerosols
654   using a shape mixture of randomly oriented polydisperse spheroids, J. Geophys. Res. Atmospheres, 102, 16831–16847,
655   https://doi.org/10.1029/96JD02110, 1997.

656   Mishchenko, M. I., Travis, L. D., and Lacis, A. A.: Scattering, Absorption, and Emission of Light by Small Particles,
657   Cambridge University Press, 492 pp., 2002.

658   Mishchenko, M. I., Liu, L., and Videen, G.: Conditions of applicability of the single-scattering approximation, Opt. Express,
659   15, 7522, https://doi.org/10.1364/OE.15.007522, 2007.

660   Monge, M. E., Rosenørn, T., Favez, O., Müller, M., Adler, G., Abo Riziq, A., Rudich, Y., Herrmann, H., George, C., and
661   D'Anna, B.: Alternative pathway for atmospheric particles growth, Proc. Natl. Acad. Sci., 109, 6840–6844,
662   https://doi.org/10.1073/pnas.1120593109, 2012.

663   Müller, D., Veselovskii, I., Kolgotin, A., Tesche, M., Ansmann, A., and Dubovik, O.: Vertical profiles of pure dust and mixed
664   smoke–dust plumes inferred from inversion of multiwavelength Raman/polarization lidar data and comparison to AERONET
665   retrievals and in situ observations, Appl. Opt., 52, 3178, https://doi.org/10.1364/AO.52.003178, 2013.

666   Nousiainen, T.: Optical modeling of mineral dust particles: A review, J. Quant. Spectrosc. Radiat. Transf., 110, 1261–1279,
667   https://doi.org/10.1016/j.jqsrt.2009.03.002, 2009.

668   Ryder, C. L., Highwood, E. J., Rosenberg, P. D., Trembath, J., Brooke, J. K., Bart, M., Dean, A., Crosier, J., Dorsey, J.,
669   Brindley, H., Banks, J., Marsham, J. H., McQuaid, J. B., Sodemann, H., and Washington, R.: Optical properties of Saharan
670   dust aerosol and contribution from the coarse mode as measured during the Fennec 2011 aircraft campaign, Atmospheric
671   Chem. Phys., 13, 303–325, https://doi.org/10.5194/acp-13-303-2013, 2013.

672   Ryder, C. L., Highwood, E. J., Walser, A., Seibert, P., Philipp, A., and Weinzierl, B.: Coarse and giant particles are ubiquitous
673   in Saharan dust export regions and are radiatively significant over the Sahara, Atmospheric Chem. Phys., 19, 15353–15376,
674   https://doi.org/10.5194/acp-19-15353-2019, 2019.

675   Sakai, T., Nagai, T., Zaizen, Y., and Mano, Y.: Backscattering linear depolarization ratio measurements of mineral, sea-salt,
676   and ammonium sulfate particles simulated in a laboratory chamber, Appl. Opt., 49, 4441–4449,
677   https://doi.org/10.1364/AO.49.004441, 2010.

678   Scanza, R. A., Mahowald, N., Ghan, S., Zender, C. S., Kok, J. F., Liu, X., Zhang, Y., and Albani, S.: Modeling dust as
679   component minerals in the Community Atmosphere Model: development of framework and impact on radiative forcing,
680   Atmospheric Chem. Phys., 15, 537–561, https://doi.org/10.5194/acp-15-537-2015, 2015.

681   Schnaiter, M., Büttner, S., Möhler, O., Skrotzki, J., Vragel, M., and Wagner, R.: Influence of particle size and shape on the
682   backscattering linear depolarisation ratio of small ice crystals-cloud chamber measurements in the context of contrail and cirrus
683   microphysics, Atmospheric Chem. Phys., 12, 10465–10484, https://doi.org/10.5194/acp-12-10465-2012, 2012.

684   Shurcliff, W. A.: Polarized Light: Production and Use, 1962.

685   Sugimoto, N. and Lee, C. H.: Characteristics of dust aerosols inferred from lidar depolarization measurements at two
686   wavelengths, Appl. Opt., 45, 7468–7474, https://doi.org/10.1364/AO.45.007468, 2006.

687   Tesche, M., Ansmann, A., Müller, D., Althausen, D., Engelmann, R., Freudenthaler, V., and Groß, S.: Vertically resolved
688   separation of dust and smoke over Cape Verde using multiwavelength Raman and polarization lidars during Saharan Mineral
689   Dust Experiment 2008, J. Geophys. Res., 114, https://doi.org/10.1029/2009JD011862, 2009.

690 Tesche, M., Kolgotin, A., Haarig, M., Burton, S. P., Ferrare, R. A., Hostetler, C. A., and Mueller, D.: 3+2 + X: what is the
691 most useful depolarization input for retrieving microphysical properties of non-spherical particles from lidar measurements
692 using the spheroid model of Dubovik et al. (2006)?, 2019.

693 Weinzierl, B., Ansmann, A., Prospero, J. M., Althausen, D., Benker, N., Chouza, F., Dollner, M., Farrell, D., Fomba, W. K.,
694 Freudenthaler, V., Gasteiger, J., Groß, S., Haarig, M., Heinold, B., Kandler, K., Kristensen, T. B., Mayol-Bracero, O. L.,
695 Müller, T., Reitebuch, O., Sauer, D., Schäfler, A., Schepanski, K., Spanu, A., Tegen, I., Toledano, C., and Walser, A.: The
696 Saharan Aerosol Long-Range Transport and Aerosol–Cloud-Interaction Experiment: Overview and Selected Highlights, Bull.
697 Am. Meteorol. Soc., 98, 1427–1451, https://doi.org/10.1175/BAMS-D-15-00142.1, 2017.

698 Winker, D. M., Vaughan, M. A., Omar, A., Hu, Y., Powell, K. A., Liu, Z., Hunt, W. H., and Young, S. A.: Overview of the
699 CALIPSO Mission and CALIOP Data Processing Algorithms, J. Atmospheric Ocean. Technol., 26, 2310–2323,
700 https://doi.org/10.1175/2009JTECHA1281.1, 2009.

701 Wiscombe, W. J. and Mugnai, A.: Single scattering from nonspherical Chebyshev particles: a compendium of calculations,
702 1986.

703 Zong, R., Weng, F., Bi, L., Lin, X., Rao, C., and Li, W.: Impact of hematite on dust absorption at wavelengths ranging from
704 0.2 to 1.0 µm: an evaluation of literature data using the T-matrix method, Opt. Express, 29, 17405–17427,
705 https://doi.org/10.1364/OE.427611, 2021.

706 Zubko, E., Muinonen, K., Muñoz, O., Nousiainen, T., Shkuratov, Y., Sun, W., and Videen, G.: Light scattering by feldspar
707 particles: Comparison of model agglomerate debris particles with laboratory samples, J. Quant. Spectrosc. Radiat. Transf.,
708 131, 175–187, https://doi.org/10.1016/j.jqsrt.2013.01.017, 2013.

709